

## 8.2 Two types of acicular ferrite

### 8.2.1 Structure with parallel laths

There appeared to be two types of acicular ferrite laths that were observed in those alloys cooled with a rapid cooling rate of  $47\text{ }^{\circ}\text{C}\text{s}^{-1}$  after the hot rolling. Diaz-Fuentes<sup>[78]</sup> has also found similarly two types of acicular ferrite by isothermal treatment in a medium carbon steel. Figure 8.13 shows some parallel laths in a lath colony in which some parallel laths interweave with one another. This can be clearly seen in figures 8.13 and 8.14. The apparent preferred habit plane of the laths in colony 1 appears to be different from that of the nearby colony 2 in figure 8.13. Combining this conclusion with the optical micrographs of this alloy (in figure 7.29), these parallel laths are possibly not from a bainite structure. This conclusion is based on no grain boundaries that can be observed in optical metallography (figure 7.29), and no cementite within the laths or on interlath positions by TEM. Acicular ferrite nucleates intragranularly on inclusions<sup>[71,74,136,137]</sup> in weld pools and not intergranularly, while its nucleation may possibly also be enhanced by dislocations resulting from prior deformation, as was described in section 7.5. The different parallel laths are possibly primary laths which have the same growth direction<sup>[75]</sup> and with a secondary lath that may nucleate at the tip of the primary one but with both having the same habit plane and orientation, resulting in a parallel sheaf morphology.

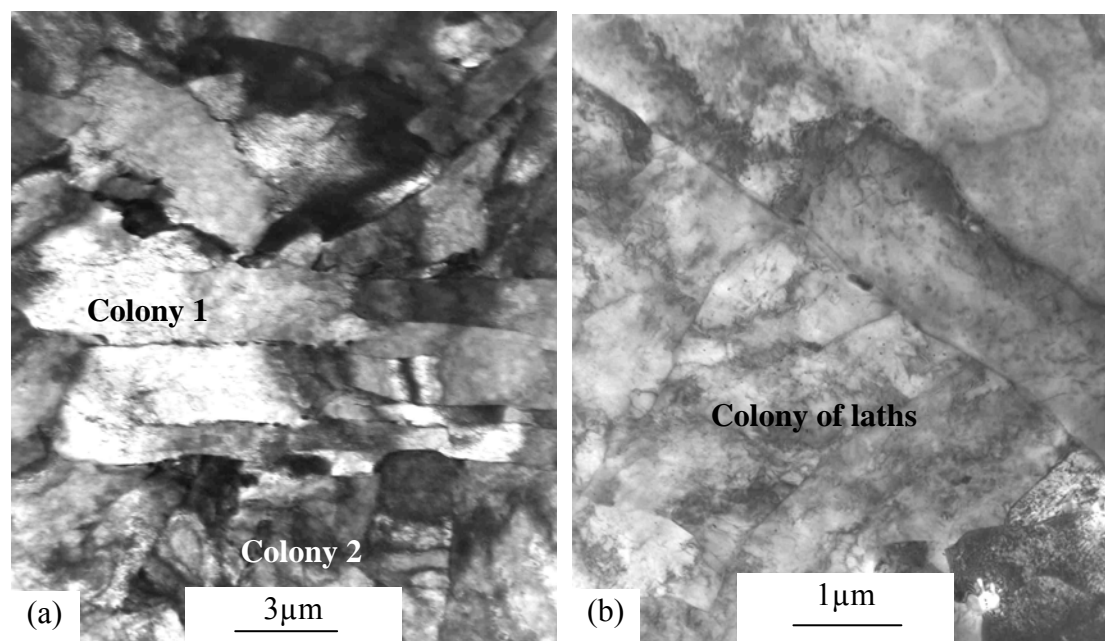


Figure 8.13 Parallel lath morphology in a colony in alloy #3 after rapid cooling at a rate of  $47\text{ }^{\circ}\text{C}\text{s}^{-1}$  after the hot rolling process.

Madariaga and Bhadeshia<sup>[75]</sup> reported a similar parallel lath morphology of acicular ferrite in a medium carbon micro-alloyed steel that was isothermally treated at a relatively low temperature of  $400\text{ }^{\circ}\text{C}$ . The two reasons given by the authors for the formation of a parallel lath microstructure are:

- (1) The lower stability of the austenite with low carbon enrichment close to the ferrite tip rather than on the face of the lath, leading to the secondary plate of ferrite nucleating at the tip of previous one.
- (2) Madariaga<sup>[75]</sup> reported that some retained austenite and cementite was found between the ferrite platelets. In that case, there was enough time for diffusion of carbon after the acicular ferrite formation because of the isothermal treatment. The excess carbon in acicular ferrite may be rejected into the austenite after the acicular ferrite formation and the cementite can be formed from the carbon-enriched austenite during this continued isothermal treatment. The austenite close to the face of the platelet has more carbon than the tip and as a result, cementite is distributed differently in the different sections of the boundary between adjacent platelets.

On the contrary, however, the parallel laths found in this study appear to be different from those in Madariaga's study<sup>[75]</sup>. No cementite was observed here on boundaries between laths or within the laths in any of the alloys in this study. Furthermore, the phase transformation in this study must have taken place in a few seconds due to the rapid cooling rate of  $47\text{ }^{\circ}\text{C}\text{s}^{-1}$ , far less than in any isothermal treatment as was used by Madariaga. Consequently, the nucleation and growth of laths in the alloys studied here are probably different from those in Madariaga's study. The nucleation of a secondary lath is dependent not only on the carbon depletion into the parent austenite in front of the interface with the primary lath (the excess carbon from the primary lath will be rejected into the adjacent austenite<sup>[75,78]</sup>, which then is not suited for the formation of a secondary lath), but also on the defects in the austenite adjacent to the primary lath, which resulted from the hot rolling process below the  $T_{nr}$ . These defects, therefore,

assist in the nucleation of the ferrite nuclei<sup>[134]</sup>. On the other hand, the secondary lath was possibly formed heterogeneously along the primary one in order to decrease the activation energy of transformation. A set of parallel laths that composes a colony, is typical of acicular ferrite found in this study. The boundary between the colonies could not be observed under the optical microscope (figure 7.29) because the size of the colonies was too small and the orientation differences between colonies were chaotic. The morphology at the end of the laths in figure 8.14 may not support the assumption that they had nucleated on the boundary of the austenite.

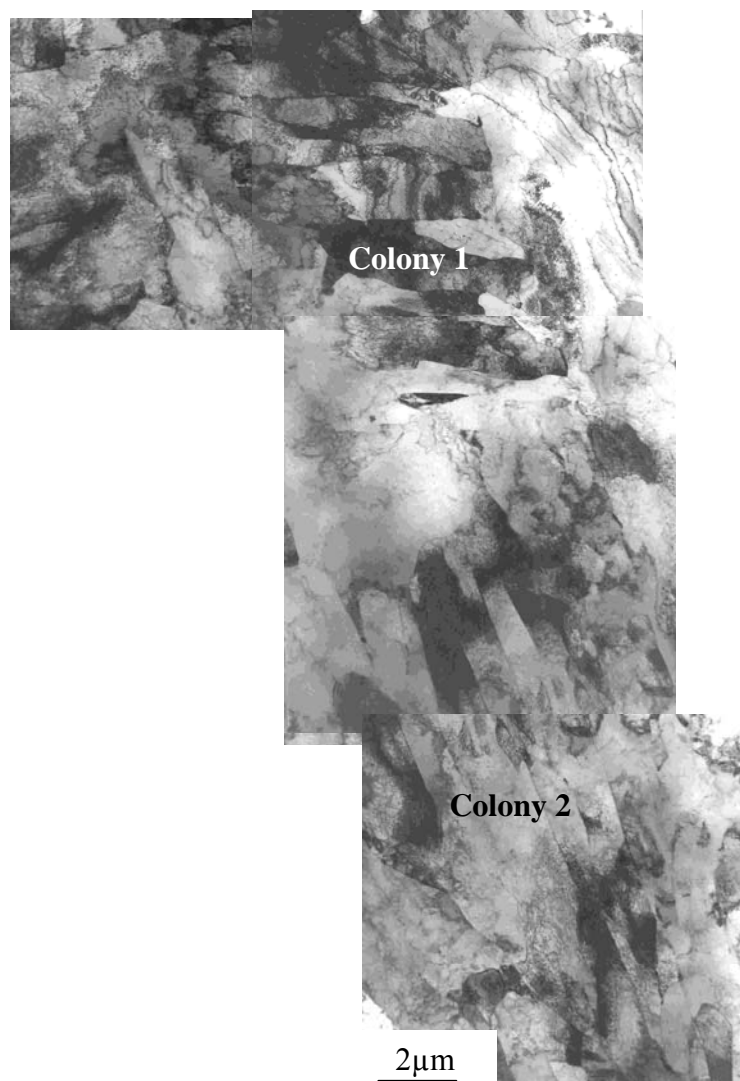


Figure 8.14 Interwoven arrangement between lath colonies in alloy #4 after a fast cooling rate of  $47\text{ }^{\circ}\text{C}\text{s}^{-1}$  after the hot rolling process.

### 8.2.2 Structure with interwoven laths

Another type of lath structure may be seen in figures 8.15 and 8.16. Laths are chaotically arranged and interwoven in between each other (marked with A, B, C, D, E and F). Each lath had its own apparent growth direction. This lath morphology appears to be the same<sup>[69,90,134]</sup> as that which other researchers have observed in welds in which many non-metallic inclusions in the weld pool act as high density nucleation sites for acicular ferrite<sup>[57,81,138]</sup>. Such a nucleation process will result in various orientations, interwoven in the nature of acicular ferrite formation.

Although there were relatively few non-metallic inclusions in the alloys in the present study, some interwoven laths were still observed even though this was not typical acicular ferrite morphology in these alloys. Where this did occur, the primary acicular ferrite (AF) lath may have nucleated on an inclusion with the next lath then nucleated on the face of the previous lath, i.e. on the interface of the primary AF lath and the untransformed austenite. The direction of growth will favour the direction in which the retarding forces of the transformation are the lowest. Figure 8.15 shows that laths B, C and F apparently nucleated on the face of lath A, while lath G probably nucleated on lath F.

It, therefore, may be concluded that there are two types of laths of acicular ferrite present in the alloys studied in this work, namely, parallel and interwoven laths with the former being the dominant type.

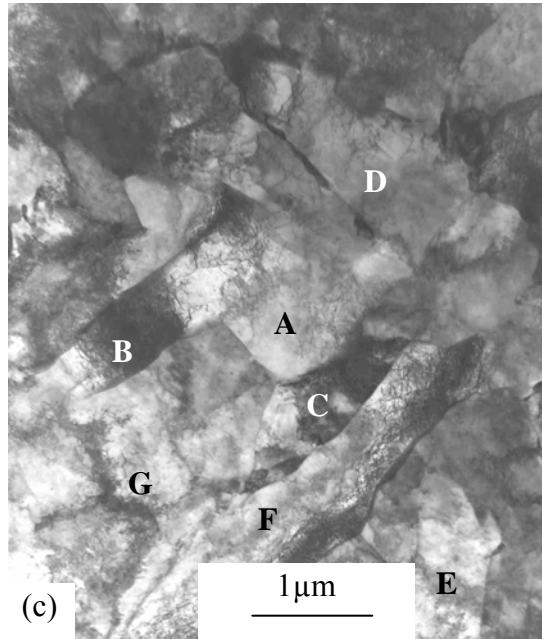


Figure 8.15 Interwoven laths micrographs in alloy #3 after fast cooling of  $47\text{ }^{\circ}\text{C}\text{s}^{-1}$  after hot rolling process.



Figure 8.16 Acicular ferrite morphology in alloy #5 after fast cooling of  $47^{\circ}\text{C s}^{-1}$  after the hot rolling process.

### 8.3 Nucleation of acicular ferrite

#### 8.3.1 Nucleation on non-metallic inclusions

Both acicular ferrite and bainite have a lath-like structure when observed in thin foil samples by Transmission Electron Microscopy, i.e. both belong to a group of transformations that proceed basically by a displacive mechanism<sup>[139]</sup>. The main differences between the nucleation and growth of these two phases are the nucleation sites and the presence of cementite inside the laths or at inter-lath positions. Bainite nucleates on an austenite grain boundary<sup>[65,66,78]</sup>, forming sheaves of parallel plates or laths with all essentially of the same crystallographic orientation. The boundaries and the general orientation of the plates are generally visible by optical microscopy (see figure 7.21-(k) in section 7.4 above).

The nucleation of an acicular ferrite structure, on the other hand, generally occurs intragranularly and often on non-metallic inclusions<sup>[70,136]</sup> as found in weld pools. As described in section 8.4, the morphologies found in this study were either parallel laths (figure 8.13) or interwoven laths (figure 8.15). Such intricate structural features, however, could not be identified by optical microscopy (see figure 7.29 in section 7.9) because of a lack of resolution of visible boundaries<sup>[131,135,140]</sup>. No precipitation of cementite was also found by thin foil TEM between or within the laths of the acicular ferrite. Accordingly, the lath morphologies in the present work differ significantly from that of bainite. These differences stem basically from differences in their nucleation mechanisms. Such differences in nucleation sites between bainite and acicular ferrite formation were also found by other authors<sup>[65,66,78,134]</sup>. A reduction of the austenite grain boundary surface area per unit volume, favours the formation of acicular ferrite and is detrimental to the formation of bainite due to the decrease in the number of potential bainite nucleation sites<sup>[65]</sup> on the austenite grain boundaries. A similar result in enhancing acicular ferrite formation was achieved by increasing the quantity of inclusions in the steel<sup>[141]</sup>. It has, therefore, been generally accepted that inclusions are the favoured sites for the nucleation of acicular ferrite<sup>[53,54,84,141,142]</sup>, at least in the case of weld pools.

As described in section 8.3 above, the microstructures of the alloys studied here consisted in general of a mixture of acicular ferrite plus polygonal ferrite. An attempt

was made to find any non-metallic inclusions that existed within the laths. Figures 8.17 to 8.20 show acicular ferrite laths around such non-metallic inclusions. The analysis by Energy Dispersive Spectroscopy (EDS) on the TEM of the inclusion in figure 8.17-(a) showed that it consisted of manganese and iron oxides. The iron peak in figure 8.17-(b) was not thought to arise entirely from the steel matrix as the size of the inclusion of about  $1.1 \mu\text{m}$  was large enough for the electron beam to strike primarily on the inclusion during the EDS analysis, although the beam had to penetrate through some matrix material to arrive at the inclusion. No diffraction pattern could be obtained on the TEM as the inclusion was too thick. The inclusion was centered inside the 50 to  $80 \mu\text{m}$  thickness of the thin foil which made it even more difficult for the electron beam to transmit through the inclusion. Consequently, any information on the structure or molecular formula of the inclusion could not be obtained from a diffraction pattern.

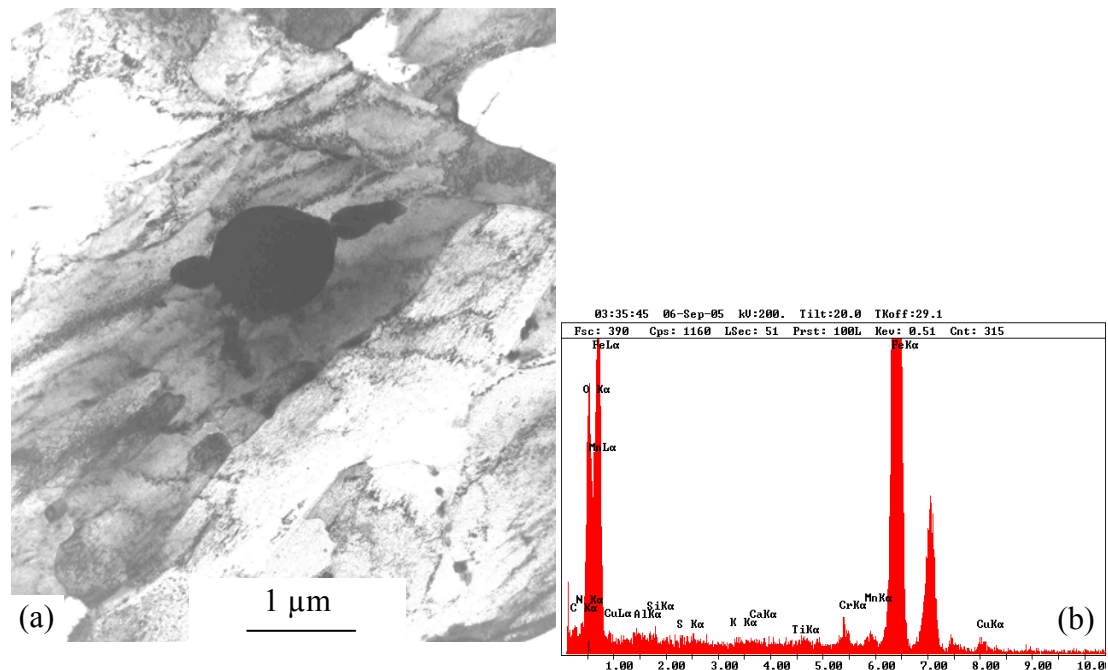


Figure 8.17 (a) TEM image of acicular ferrite and a large non-metallic inclusion in alloy #5 after a rapid cooling rate of  $47 \text{ }^\circ\text{C s}^{-1}$  after the hot rolling, (b) EDS analysis on the inclusion in this figure (a).

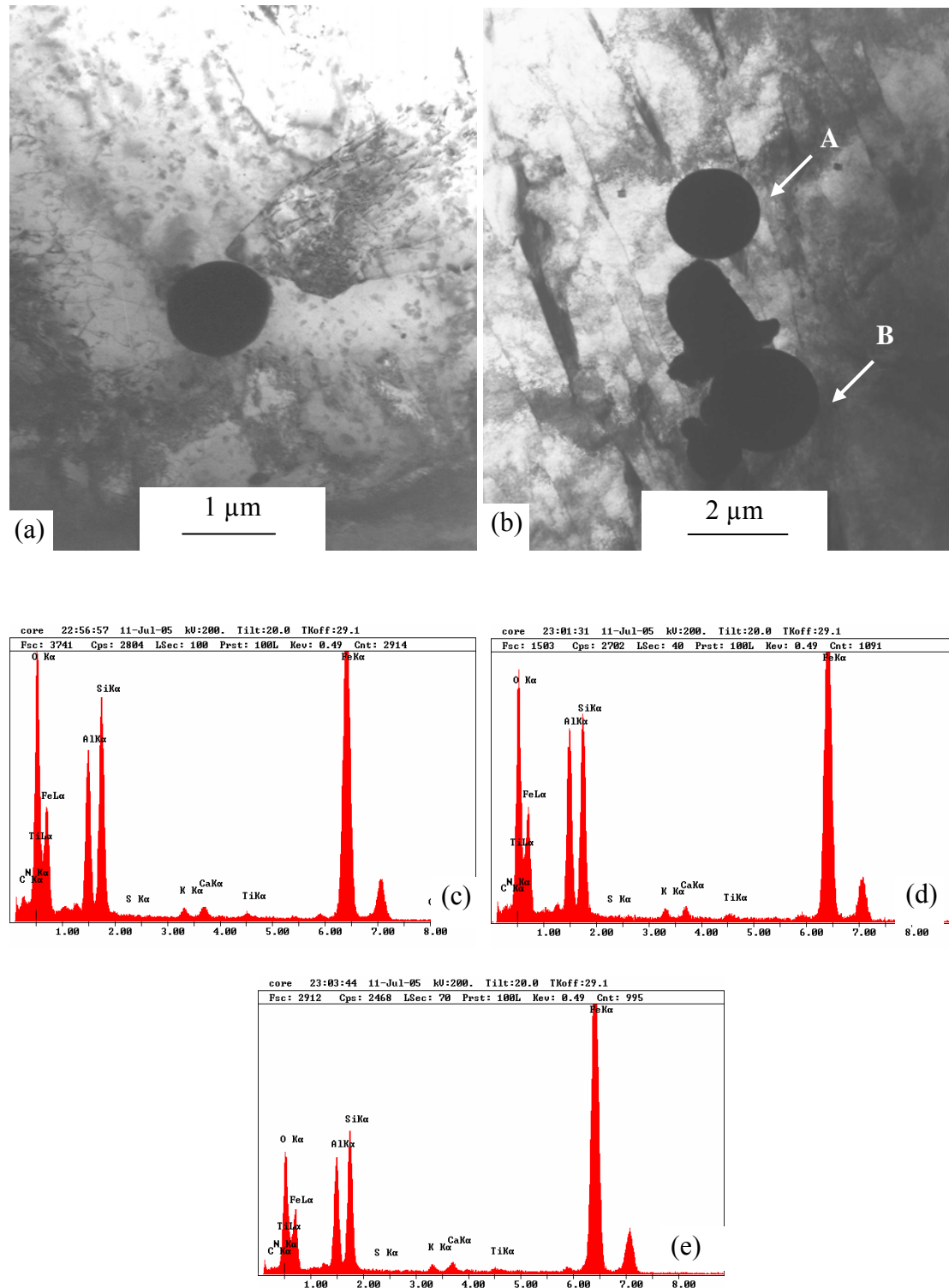


Figure 8.18 Laths nucleated on non-metallic inclusions (a) in alloy #1 after a rapid cooling rate of  $47\text{ }^{\circ}\text{C}\text{s}^{-1}$  after the hot rolling, (b) in alloy #3 after a rapid cooling rate of  $40\text{ }^{\circ}\text{C}\text{s}^{-1}$  from  $980\text{ }^{\circ}\text{C}$  down to room temperature without deformation, (c) EDS analysis on the inclusion in this figure (a), (d) and (e) EDS analysis on the inclusions A and B in this figure (b), respectively.

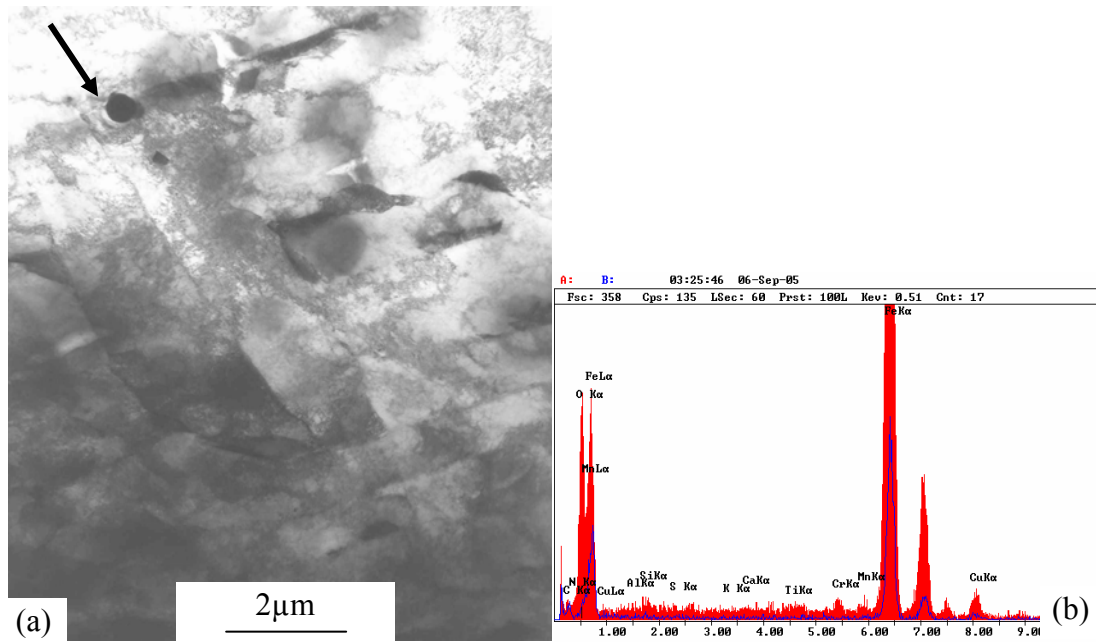


Figure 8.19 (a) Nucleation of interwoven laths of acicular ferrite in sample #AF3F of alloy #3 after a cooling rate of  $20 \text{ }^{\circ}\text{C s}^{-1}$  from  $980 \text{ }^{\circ}\text{C}$  down to room temperature without deformation, (b) EDS analysis of red peak was from on the inclusion indicated by an arrow in this figure (a), while blue peak was from the matrix steel.

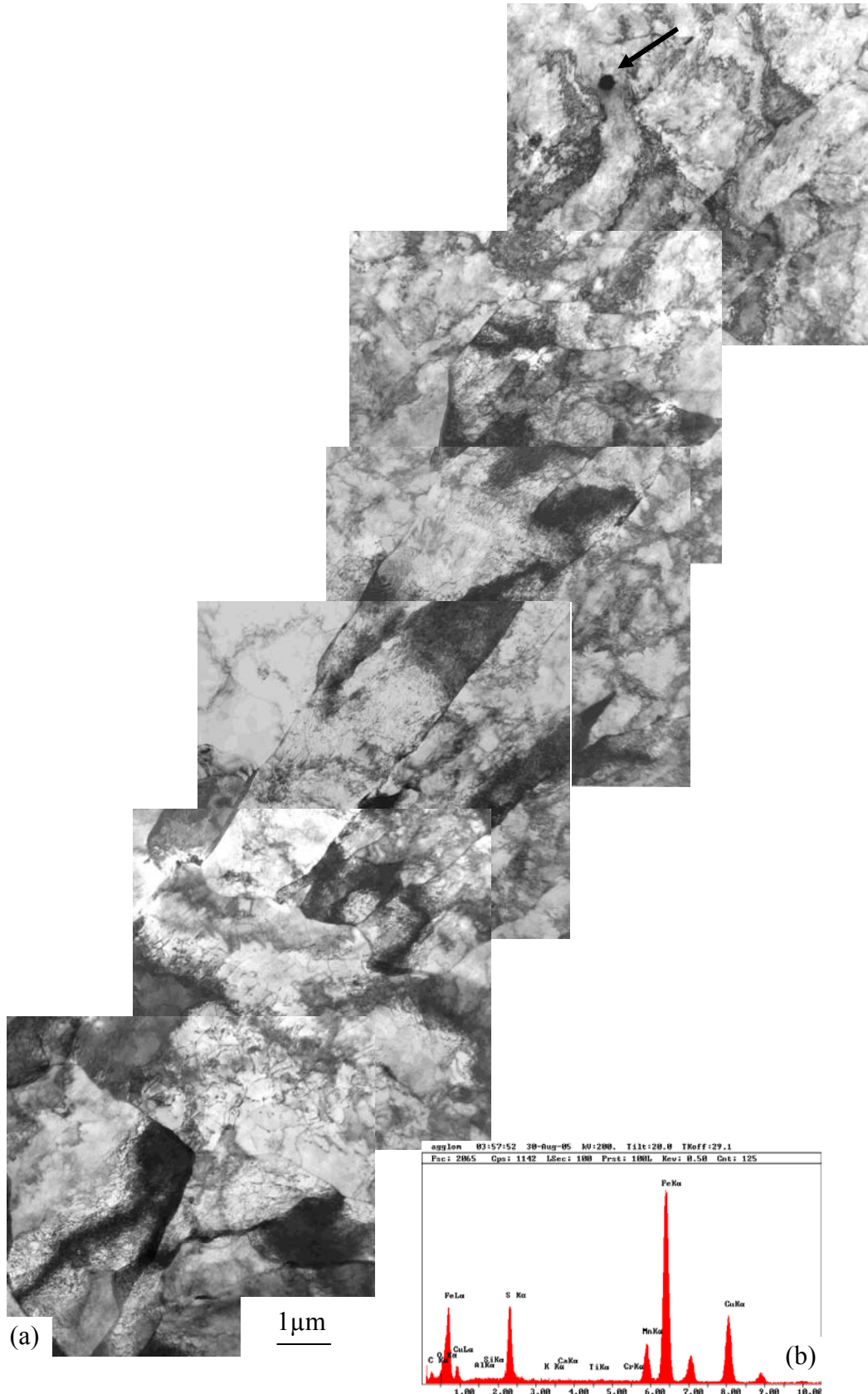


Figure 8.20 (a) Non-metallic inclusion and acicular ferrite in alloy #3 after a rapid cooling rate of  $47\text{ }^{\circ}\text{C}\text{s}^{-1}$  after the hot rolling, (b) EDS analysis on the inclusion indicated by an arrow in this figure (a).

Similar nucleation of laths of acicular ferrite on inclusions was also found in alloy #1 (figure 8.18-(a) above). The inclusions in this case were generally round in shape, with a size of about 1.2  $\mu\text{m}$ . The EDS image in figure 8.18-(c) reveals that the composition of these inclusions was apparently a complex oxide containing silicon, aluminium and iron.

Further nucleation of acicular ferrite on non-metallic inclusions is shown in figure 8.18-(b) for sample #AF3F of alloy #3 (0.09% Mo) that was cooled at 40  $^{\circ}\text{C}\text{s}^{-1}$  from 980 $^{\circ}\text{C}$  down to room temperature (figure 6.14 in section 6.9). The acicular ferrite had once more, a typical lath structure nucleated around non-metallic inclusions with rounded shapes. The diameter of the inclusions ranged from 1.9  $\mu\text{m}$  to 2.2  $\mu\text{m}$  (see figure 8.18-(b)). The EDS image in figure 8.18-(d) and (e) revealed that they were complex oxides containing silicon, aluminium and iron. From the figure it appears that the two primary parallel laths of acicular ferrite nucleated on the non-metallic inclusion. The secondary lath, however, nucleated at the tip of the primary one, possibly owing to a lower carbon content in this area and then grew in the same direction as the primary one.

The nucleation of interlocked laths of acicular ferrite is shown in figure 8.19 for another sample in group #AF3F of alloy #3 (0.09% Mo) (figure 6.14 in section 6.9). The cooling rate was 20  $^{\circ}\text{C}\text{s}^{-1}$  from 980  $^{\circ}\text{C}$  down to room temperature. The inclusions were about 0.5  $\mu\text{m}$  in diameter and, therefore, quite small to be analysed with confidence by EDS in the thin foil. The blue peak for iron in figure 8.19-(b) probably arose from the matrix of the steel surrounding the inclusion. There is a difference in the iron peak between the red and blue lines in the EDS image. Therefore, it appears that the non-metallic inclusion shown by an arrow in the figure was a mixture of manganese, iron and copper oxide.

Figure 8.20 shows the nucleation of an acicular ferrite colony on an inclusion of about 0.35  $\mu\text{m}$  in diameter. For such an inclusion, the iron peak in figure 8.20-(b) is probably from the steel matrix and not from the inclusion. Thus, the acicular ferrite nucleated on an inclusion consisting probably of manganese and copper sulphide.

Summarising the results above, a number of inclusions were found that were associated with acicular ferrite laths. Previous researchers have also found that acicular ferrite nucleates on non-metallic inclusions<sup>[75,77,141]</sup> and their nucleation frequency increases with an increasing quantity of inclusions in a weld pool<sup>[141,143]</sup>. In this work the nucleation sites for acicular ferrite were generally oxide and sulphide inclusions with generally a rounded shape whereas the size of these inclusions ranged from 0.35 to 2.2  $\mu\text{m}$ . The chemical compositions of these non-metallic inclusions were complex containing silicon, aluminium, iron, manganese and copper.

### 8.3.2 Type of non-metallic inclusion as nucleants

Other researchers have reported that acicular ferrite nucleates on inclusions or particles, such as  $\text{TiO}$ <sup>[141,144,145]</sup>, BN plus rare earth metal oxysulphides<sup>[148]</sup>, aluminium-rich inclusions<sup>[147,148]</sup>, and  $\text{TiN}$ <sup>[149]</sup>. Most of the work, however, focused on weld pools where a larger quantity of non-metallic inclusions is readily introduced. Bhatti<sup>[147]</sup> has reported that inclusions rich in manganese and inclusions covered by a skin of sulphide are ineffective nucleants for acicular ferrite. Inclusions which are covered by or are rich in copper-sulphur or silicon and which were effective as a nucleant<sup>[65,66,70]</sup> for acicular ferrite, however, were found by Zhang and Farrar<sup>[141]</sup>, Dowling et al<sup>[144]</sup>, Court<sup>[150]</sup>, Harbottl<sup>[151]</sup>, Madariaga<sup>[69]</sup> and Kayali et al<sup>[152]</sup>. Similar oxide inclusions of manganese plus iron and containing copper and also manganese sulphides containing copper have been found in this work (see figures 8.19 and 8.20 respectively). It may, therefore, be concluded that the type of inclusions that had formed nucleation sites for acicular ferrite in these steels studied here, were most likely complex oxides or sulphides.

### 8.3.3 Nucleation mechanisms of acicular ferrite

Three nucleation mechanisms of acicular ferrite on inclusions have been proposed by previous researchers: (1) the existence of local variations in the chemistry of the matrix<sup>[90]</sup>; (2) the generation of high strain fields around the inclusion due to the different thermal expansion coefficients between austenite and the inclusion<sup>[153,154]</sup> or deformation in the austenite region; and (3) the creation of a low energy interface between acicular ferrite and the inclusion owing to a low lattice mismatch between them<sup>[69, 155-158]</sup>.

When acicular ferrite is formed, the total system's Gibbs free energy must be lowered for the nucleus to become thermodynamically stable. This total energy includes the decrease in the chemical free energy, the disappearance of an interface between the inclusion and the austenite, and two new interfaces created of austenite-acicular ferrite and inclusion-acicular ferrite. This change in total energy can be described by the following equation:

$$\Delta G_{\text{total}} = -\Delta G_v V_{\text{AF}} + \sigma_{\text{AF}/\gamma} A_{\text{AF}/\gamma} + \sigma_{\text{AF}/\text{I}} A_{\text{AF}/\text{I}} + \Delta G_\epsilon V_{\text{AF}} - \sigma_{\text{I}/\gamma} A_{\text{I}/\gamma} - \Delta G_{\text{defect}} V_{\text{AF}} \quad (8.1)$$

where  $\Delta G_v$  is the decrease in Gibbs free energy per unit volume owing to the transformation from austenite to acicular ferrite, also often termed the “chemical free energy”,

$V_{\text{AF}}$  is the volume of transformed acicular ferrite,

$\sigma_{\text{AF}/\gamma}$ ,  $\sigma_{\text{AF}/\text{I}}$ ,  $\sigma_{\text{I}/\gamma}$  are interface energies per unit area between acicular ferrite and austenite, acicular ferrite and an inclusion and an inclusion and austenite, respectively;  $A_{\text{AF}/\gamma}$ ,  $A_{\text{AF}/\text{I}}$ ,  $A_{\text{I}/\gamma}$  are the interface areas between acicular ferrite and austenite, acicular ferrite and an inclusion and, an inclusion and austenite, respectively,

$\Delta G_\epsilon$  is the strain energy per unit volume around the new AF nucleus due to the volume expansion during the transformation from a face-centered cubic lattice (fcc) to a body-centered cubic lattice (bcc) and

$\Delta G_{\text{defect}}$  is the stored defect elastic energy per unit volume in austenite around the inclusion due to deformation in the austenite, such as dislocation or point defects.

$-\Delta G_v V_{\text{AF}}$  is the chemical Gibbs driving force for the transformation that is dependent on the degree of under-cooling of the austenite as well as the chemical composition of the austenite and is generally independent of the inclusions present in the austenite.

$\sigma_{\text{AF}/\text{I}} A_{\text{AF}/\text{I}}$  and  $\sigma_{\text{I}/\gamma} A_{\text{I}/\gamma}$  are only affected by inclusions where acicular ferrite nucleates and is primarily determined by the mismatch of the interface between acicular ferrite and an inclusion. The transformation will proceed more readily through an increasing absolute value of  $-\Delta G_v V_{\text{AF}}$  and become stable when the embryo size of acicular ferrite ( $r$ ) reaches the critical size ( $r^*$ ) ( $r^*$  is determined according to  $\frac{d\Delta G_{\text{total}}}{dr} = 0$ ). This

driving force is increased by increasing the under-cooling  $\Delta T$  which again is increased by a higher cooling rate on the rising part of the “nose” on a CCT diagram. That this

is so, is confirmed by the results shown on the CCT diagrams in figures 7.26 and 7.28 in section 7.5 where it was found that a faster cooling rate after deformation of the austenite is more favourable for acicular ferrite formation because the under-cooling increases with an increase in cooling rate.

$\sigma_{AF/\gamma}A_{AF/\gamma}$ ,  $\sigma_{AF/I}A_{AF/I}$  and  $\Delta G_e V_{AF}$  are the barriers to the nucleation of AF. It means that low values of the surface energies  $\sigma_{AF/\gamma}$  and  $\sigma_{AF/I}$  are beneficial to the nucleation of acicular ferrite on inclusions.  $\sigma_{AF/\gamma}$  is dependent on the crystal lattice mismatch between acicular ferrite and austenite and will, therefore, determine the crystallographic orientation of the laths. For instance, a low  $\sigma_{AF/\gamma}$  will arise from a low lattice mismatch between them.

In the present case where a lack of sufficient inclusions in the steels may occur, the typical acicular ferrite will be the parallel lath structure due to a low mismatch between austenite and acicular ferrite (also leading to a low  $\sigma_{AF/\gamma}$ ) in this direction which is parallel to the primary one.  $\sigma_{AF/I}$ , however, is dependent on the lattice structure of the inclusion. An inclusion that has a lower mismatch with an acicular ferrite nucleus, is favoured more to nucleate acicular ferrite. Some researchers<sup>[141,144,159]</sup> have observed that an inclusion with a manganese sulphide core covered by a skin of copper sulphide acts as a nucleant for acicular ferrite, instead of manganese sulphide only.

Considering the surface energy  $\sigma_{I/\gamma}$  between an inclusion and austenite only (which effectively becomes an additional driving force as it is removed from the system upon forming an acicular ferrite nucleus), on the other hand, this energy increases with an increase in their melting temperature<sup>[141]</sup>. The melting temperature is 1620 °C for manganese sulphide, while it is 1125 °C for copper sulphide<sup>[141]</sup>, which means that  $\sigma_{MnS/\gamma}$  is higher than  $\sigma_{CuS/\gamma}$ , and this will result in manganese sulphide being a more effective nucleant than copper sulphide as it provides a higher additional driving force. However, Evans<sup>[160]</sup> has reported that a high lattice mismatch exists between

manganese sulphide and ferrite, leading to a high retarding force  $\sigma_{\text{MnS/AF}}$ . Therefore, copper sulphide may be more favourable to nucleate acicular ferrite than manganese sulphide owing to the lower mismatch between it and the ferrite<sup>[65]</sup>. A similar inclusion has also been found in the present study in alloy #3 (see figure 8.20). It is believed that the inclusion may possibly also have been manganese sulphide in the core and copper sulphide on the outer skin although the difference between core and skin were not resolved by EDS owing to the small size of the inclusion. Accordingly, it can only be speculated that the surface layer of this inclusion may have been favourable for the nucleation of acicular ferrite as found by others for such types of inclusions.

As indicated above,  $-\sigma_{\text{I}/\gamma}A_{\text{I}/\gamma}$  is another driving force for the transformation because of its negative sign. A high energy interface would preferably be replaced by a low energy one during the phase transformation, thus lowering the effective energy barrier for nucleation according to classical nucleation theory. Using the general assumption that the interface energy of phases or particles increase with their melting temperature, Dowling<sup>[144]</sup> has proposed that  $\text{Al}_2\text{O}_3$  and  $\text{SiO}_2$  would be expected to have high interface energies. These inclusions would, therefore, be efficient nucleants for acicular ferrite. In this work some aluminium, silicon and manganese oxides were found within the acicular ferrite laths (see figures 8.17 to 8.19) which were effective nucleants because these inclusions are of higher melting temperatures, 2015 °C for  $\text{Al}_2\text{O}_3$ , 1713 °C for  $\text{SiO}_2$  and 1650 °C for  $\text{MnO}$ <sup>[65]</sup>.

The additional driving force  $-\Delta G_{\text{defect}}$  arises from any defects in the austenite around inclusions from the deformation in the parent austenite during hot rolling below the  $T_{\text{nr}}$ . Most of these defects are likely to be dislocations as point defects will probably already anneal out during the hot rolling, even below the  $T_{\text{nr}}$ . The total strain in the finish rolling process below the  $T_{\text{nr}}$  of 0.54 that was applied here, would have resulted in a relatively high dislocation density within the austenite at the point of deformation. Furthermore, the density of dislocations immediately around inclusions will be higher than further away because of a concentration in deformation behaviour in the austenite in those areas. That this is likely to occur, has been shown by a number of authors in the theory of Particle Stimulated Nucleation (PSN) around large

precipitates after cold working in aluminium alloys<sup>[97]</sup>. In the PSN theories<sup>[161,162]</sup>, it has been shown that the deformation zones around large second phase particles contain a larger number of “geometrically necessary” dislocations than further away and this leads to a higher driving force for nucleation during recrystallisation at the surfaces of these particles.

Similar to the above case of PSN, a higher stored defect energy, therefore, possibly exists in the area of austenite around an inclusion than further away or in undeformed austenite. This stored energy provides an additional driving force for acicular ferrite nucleation. It also means that the nucleation barrier for acicular ferrite may be reduced in the strain and dislocation field around the inclusion, leading to the observation that deformation in the austenite accelerates the nucleation of acicular ferrite or generates suitable nucleation sites<sup>[134,141]</sup>. This point has been demonstrated clearly by the results of the strain affected CCT diagrams in this study, in which it was demonstrated in section 7.5 that deformation in the austenite is beneficial to acicular ferrite formation instead of bainite.

$\Delta G_e V_{AF}$  is another retarding force of strain energy due to the volume expansion during the transformation because there is a lattice change from fcc (austenite) to bcc (acicular ferrite). The amount of this strain energy is dependent on the temperature of the transformation and lower transformation temperatures will result in a higher strain energy because the untransformed austenite around acicular ferrite will strain harden more than at higher temperatures.

Acicular ferrite, however, is a displacive transformation and it is also possible that defects in the austenite prior to the transformation that may promote the nucleation, can also retard the growth<sup>[76]</sup>. The nucleated primary laths formed around inclusions may, therefore, grow to a smaller size in deformed austenite (see figure 7.27 of alloy #5 in section 7.5) than in a well annealed austenite. This will result in an overall finer ferrite grain size after transformation. A coarse acicular ferrite microstructure was only observed in alloy #5 without prior deformation (figure 7.23 in section 7.4).

In summary, therefore, deformation in the austenite prior to the transformation appears to accelerate the nucleation of acicular ferrite and thereafter possibly limits its growth, so that the size of the formed acicular ferrite packets or grains becomes finer.